Journal of Computational and Applied Mathematics 451 (2024) 116105

Contents lists available at ScienceDirect

Journal of Computational and Applied Mathematics

journal homepage: www.elsevier.com/locate/cam

Theoretical and numerical study of case reporting rate with application to epidemiology

Alexandra Smirnova [*,1], Mona Baroonian

Department of Mathematics & Statistics, Georgia State University, Atlanta, USA

ARTICLE INFO

Keywords:
Epidemiology
Incidence reporting rate
Convergence analysis
Transmission dynamic
Regularization algorithm

ABSTRACT

A clear understanding of actual infection rate is imperative for control and prevention of diseases. In particular, it helps in formulating effective vaccination strategies and in assessing the level of herd immunity required to contain the virus. In this paper, we conduct theoretical and numerical study of a novel optimization procedure aimed at stable estimation of incidence reporting rate and time-dependent effective reproduction number from real data on new incidence cases, daily new deaths, and vaccination percentages. The iteratively regularized optimization algorithm can be applied to a broad class of data fitting problems constrained by various biological models, where one has to account for under-reporting of cases. To that end, general nonlinear observation operators in real Hilbert spaces are considered in the proposed convergence analysis. To illustrate theoretical findings, numerical simulations with SVI_sI_vRD compartmental model and real data for Delta variant of COVID-19 pandemic in different states of the US are conducted.

1. Introduction

How widely has the virus spread? This important and often overlooked question was brought to light by the recent COVID-19 outbreak. Several techniques have been used to account for silent spreaders along with varying testing and healthcare seeking habits as the main reasons for under-reporting of COVID-19 cases. It has been observed that silent spreaders play a more significant role in disease progression than previously understood, highlighting the need for policymakers to incorporate these hidden figures into their strategic responses.

In [1], the real number of COVID-19 instances in Europe has been investigated based on reported daily new deaths and pre-estimated death rate (assuming it takes about 18 days from virus acquisition to death). To account for the observed irregularities, the authors considered how quickly each country detected and reported COVID-19 infections. The study in [1] suggested that the factual tally of COVID-19 cases noticeably surpassed the officially reported statistics.

The study in [2] employed the techniques of machine learning to find the incidence reporting rate by incorporating "invisible spreaders" in a modified SIR (Susceptible - Infected - Removed) model. The authors of [2] assessed the impact of invisible spreaders on the pandemic progression by varying the proportion of invisible spreaders in their numerical simulations. They discovered that even a slight rise in the percentage of invisible spreaders has the potential to significantly magnify the overall health impact on the community.

The research [3] used a modified $SEIR$ model that integrated both epidemiological and behavioral factors to address the limitations of testing, prevalence of asymptomatic cases, and reporting variations among countries until September 30, 2020. The

* Corresponding author.
E-mail addresses: asmirnova@gsu.edu (A. Smirnova), mbaroonian1@student.gsu.edu (M. Baroonian).

[1] Supported by NSF, USA award 2011622 (DMS Computational Mathematics).

https://doi.org/10.1016/j.cam.2024.116105
Received 27 December 2023; Received in revised form 12 June 2024
Available online 25 June 2024

study revealed a significant under-reporting of cases and deaths globally, with cumulative cases around 7 times higher than in official reports across 92 nations. The research underscored the challenges of assessing the true scope of the pandemic, emphasizing the need for accurate reporting and effective policy responses.

The authors of [4] utilize a networked dynamic population model together with Bayesian inference to analyze the early spread of COVID-19 in China. According to the authors' findings, around 86% of COVID-19 infections remained undocumented before travel restrictions were put in place on January 23, 2020, and before the widespread testing became available. The transmission rate of undocumented cases per person was slightly over a half the transmission rate of the documented ones. Still, due to their large number, these undocumented infections were the source of the vast majority of documented cases. This explains the rapid geographic spread of COVID-19 in early 2020 and the unique challenge of containing this virus.

In [5], numerical simulations with post-vaccination COVID-19 data have been conducted for the period from July 9 to November 25, 2021. A new optimization algorithm has been introduced to analyze the data for new incidence cases and daily deaths. The study found that during the Delta wave of the pandemic in the US, in most states the reporting rate of new COVID-19 cases was between 15% to 25%.

While the methodology for the reporting rate estimation has moved to the forefront of bioinformatics research during the COVID-19 pandemic, this topic is of paramount importance in the study of many other infectious diseases. For example, in the case of 2014 Ebola (EVD) outbreak in West Africa [6], numerous early cases have not been reported since the symptoms of the disease were similar to malaria, typhoid fever, hepatitis and other viral haemorrhagic fevers. As the result, identification of the true nature of the disease and the implementation of much needed mitigation measures were delayed. During *Vibrio cholerae* epidemic in Peru, a significant proportion of asymptomatic cases [7,8] remained underreported. The unprecedented *cholerae* outbreak started in 1991 and generated multiple waves of disease over several years. In [8], the reporting rate estimation for *cholerae* infections has been incorporated in the numerical study.

A clear understanding of actual infection rate is imperative for control and prevention. In particular, it helps in formulating effective vaccination strategies and in assessing the level of herd immunity required to contain the virus. In this paper, we conduct theoretical and numerical study of a novel optimization procedure aimed at stable estimation of incidence reporting rate and time-dependent effective reproduction number from real data on new incidence cases, daily new deaths, and vaccination percentages. The regularized optimization algorithm can be applied to a broad class of data fitting problems constrained by various biological models, where one has to account for under-reporting of cases. To that end, in the convergence analysis we consider general nonlinear observation operators in real Hilbert spaces. To illustrate our theoretical findings, we conduct numerical simulations with real data for Delta variant of COVID-19 pandemic in different states of the US [9,10]. As a biological model for post-vaccination stage of COVID-19, we use a SVI_sI_vRD-type of transmission dynamic first introduced in [11].

The paper is organized as follows. In Section 2, we present the motivation and introduction of a new iteratively regularized optimization scheme for the reporting rate estimation. In Section 3, a rigorous theoretical analysis of the proposed algorithm, coupled with *a posteriori* stopping rule, is carried out. Numerical experiments for the SVI_sI_vRD-constrained nonlinear least squares problem are given in Section 4. Conclusions and future plans are outlined in Section 5.

2. Nonlinear constrained minimization problem

Parameter $\mathcal{R}_0$ is a widely used indicator of a transmission potential in a well-mixed susceptible population and is driven by the average contact rate and the mean infectious period of the disease [12]. Yet, it only characterizes transmission potential at the onset of the epidemic and varies geographically due to differences in local healthcare, mitigation measures, social and cultural factors [13,14]. Unlike $\mathcal{R}_0$, the effective reproduction number, $\mathcal{R}_e(t)$, tracks time-dependent changes in transmission potential during the entire course of the outbreak. Therefore, stable estimation of the effective reproduction number, $\mathcal{R}_e(t)$, and its underlying transmission rate, $\beta(t)$, is extremely important [15–17].

A time-dependent transmission rate of an epidemic, $\beta(t)$, is usually estimated from a nonlinear minimization problem constrained by a disease-specific (networked) dynamic population model, $\tilde{G}(u,\beta)=0$, with observation operators, $\tilde{\Phi}(u,\beta)$ and $\tilde{\Omega}(u,\beta)$, fitted to daily new cases and deaths, $\hat{\eta}$ and $\hat{\sigma}$, respectively. In $\tilde{G}(u,\beta)=0$, u is the state variable describing various ″states″ of a disease. Oftentimes, due to a considerable number of asymptomatic cases [18,19], one has to assume that incidence data, $\hat{\eta}$, is underreported, and the true number of incidence cases is $\hat{\eta}/\Psi$, $0<\Psi<1$. The reporting of daily new deaths, on the other hand, is more accurate for most diseases. While still noise contaminated, the data on daily new deaths, $\hat{\sigma}$, is not generally under- or over-reported. Thus, our goal is to optimize the biological model, $\tilde{G}(u,\beta)=0$, with respect to the transmission rate, $\beta=\beta(t)$, and the reporting rate, Ψ, by solving the following nonlinear least squares problem (NLSP)

$$\min_{\beta,\psi}\tilde{\Lambda}(\beta,\psi),\quad \text{where } \tilde{\Lambda}(\beta,\psi):=\frac{\lambda_1}{2}\|\tilde{\Phi}(u,\beta)-\psi\hat{\eta}\|^2+\frac{\lambda_2}{2}\|\tilde{\Omega}(u,\beta)-\hat{\sigma}\|^2,\quad \lambda_1,\lambda_2>0, \tag{2.1}$$

subject to the constraint, $\tilde{G}(u,\beta)=0$. In (2.1), the reporting index, ψ, is the reciprocal of the reporting rate, Ψ, and u is the state variable. The purpose of λ_1 and λ_2 is to balance the two residuals, since $\psi\hat{\eta}$ and $\hat{\sigma}$ are of different orders of magnitude. If one solves the constraint biological system, $\tilde{G}(u,\beta)=0$, for the state variable, u, and substitutes $u=u(\beta)$ into the observation operators, $\tilde{\Phi}(u,\beta)$ and $\tilde{\Omega}(u,\beta)$, then one arrives at an unconstrained minimization problem

$$\min_{\beta,\psi}\Lambda(\beta,\psi),\quad \text{where } \Lambda(\beta,\psi):=\frac{\lambda_1}{2}\|\Phi(\beta)-\psi\hat{\eta}\|^2+\frac{\lambda_2}{2}\|\Omega(\beta)-\hat{\sigma}\|^2,\quad \lambda_1,\lambda_2>0, \tag{2.2}$$

where $\tilde{\Phi}(u(\beta),\beta) := \Phi(\beta)$ and $\tilde{\Omega}(u(\beta),\beta) := \Omega(\beta)$. In most practically interesting cases, the population model, $\tilde{G}(u,\beta) = 0$, is nonlinear with respect to the state variable, u. Therefore, generally, the operator equation $\tilde{G}(u,\beta) = 0$ has to be solved numerically for every current value of $\beta(t) = \beta_k(t)$, $k = 1, 2, \ldots$

Assume that Fréchet differentiable observation operators Φ and Ω act between real Hilbert spaces H and H_1 and H and H_2, respectively, i.e., $\Phi : H \to H_1$ and $\Omega : H \to H_2$. By the first order necessary condition (FONC) for the unconstrained minimization, one concludes

$$\frac{\partial}{\partial\psi}\Lambda(\beta,\psi) = 0, \quad \text{that is,} \quad -(\hat{\eta},\Phi(\beta)) + \psi\|\hat{\eta}\|^2 = 0 \quad \text{and} \quad \psi = \frac{(\hat{\eta},\Phi(\beta))}{\|\hat{\eta}\|^2}, \tag{2.3}$$

where $(\,,\,)$ is a scalar product in the Hilbert space H_1. This yields the NLSP in the form

$$\min_{\beta}\left\{\frac{\lambda_1}{2}\left\|\Phi(\beta) - \frac{\hat{\eta}(\hat{\eta},\Phi[\beta])}{\|\hat{\eta}\|^2}\right\|^2 + \frac{\lambda_2}{2}\left\|\Omega(\beta) - \hat{\sigma}\right\|^2\right\}. \tag{2.4}$$

Let $\hat{v} := \dfrac{\hat{\eta}}{\|\hat{\eta}\|}$ be the normalized incidence data. Then nonlinear optimization problem (2.4) can be cast as follows

$$\min_{\beta}\left\{\frac{\lambda_1}{2}\|(E - \hat{v}(\hat{v},\cdot))\Phi(\beta)\|^2 + \frac{\lambda_2}{2}\|\Omega(\beta) - \hat{\sigma}\|^2\right\}. \tag{2.5}$$

In (2.5), E is the identity operator in H_1 and $E - \hat{v}(\hat{v},\cdot)$ is an orthogonal projection. By the FONC,

$$\lambda_1\left((E - \hat{v}(\hat{v},\cdot))\Phi'(\beta)\right)^{\top}(E - \hat{v}(\hat{v},\cdot))\Phi(\beta) + \lambda_2\Omega'^{\top}(\beta)[\Omega(\beta) - \hat{\sigma}] = 0. \tag{2.6}$$

Since $\hat{P}^2 = \hat{P} = \hat{P}^{\top}$ for $\hat{P} := E - \hat{v}(\hat{v},\cdot)$, one has $\lambda_1\Phi'^{\top}(\beta)\hat{P}\Phi(\beta) + \lambda_2\Omega'^{\top}(\beta)[\Omega(\beta) - \hat{\sigma}] = 0$. This yields the following Hessian operator:

$$H(\beta) := \lambda_1\Phi''^{\top}(\beta)\hat{P}\Phi(\beta) + \lambda_1\Phi'^{\top}(\beta)\hat{P}\Phi'(\beta) + \lambda_2\Omega''^{\top}(\beta)[\Omega(\beta) - \hat{\sigma}] + \lambda_2\Omega'^{\top}(\beta)\Omega'(\beta). \tag{2.7}$$

In transition from full Newton to Gauss–Newton, one disregards the terms containing the second derivative operator applied to the residual, since the residual is expected to decrease as iterations move forward. Thus one obtains Hessian approximation in the form

$$H(\beta) \approx \lambda_1\Phi'^{\top}(\beta)\hat{P}\Phi'(\beta) + \lambda_2\Omega'^{\top}(\beta)\Omega'(\beta). \tag{2.8}$$

This Hessian approximation is self-adjoint and nonnegative definite. Indeed, for any $h \in H$, one has

$$\begin{aligned}&\lambda_1 h^{\top}\Phi'^{\top}\hat{P}\Phi' h + \lambda_2 h^{\top}\Omega'^{\top}\Omega' h = \lambda_1 h^{\top}\Phi'^{\top}\hat{P}^{\top}\hat{P}\Phi' h + \lambda_2 h^{\top}\Omega'^{\top}\Omega' h \\ &= \lambda_1(\hat{P}\Phi' h)^{\top}\hat{P}\Phi' h + \lambda_2(\Omega' h)^{\top}\Omega' h = \lambda_1\|\hat{P}\Phi' h\|^2 + \lambda_2\|\Omega' h\|^2 \geq 0.\end{aligned} \tag{2.9}$$

Given Hessian approximation (2.8), we propose to solve minimization problem (2.5) numerically by using what we call iteratively regularized projected Gauss–Newton (IRPGN) algorithm [20–23]:

$$\begin{aligned}&P := E - v(v,\cdot), \quad \Phi_k := \Phi(\beta_k), \quad \Omega_k := \Omega(\beta_k), \quad \Phi'_k := \Phi'(\beta_k), \quad \Omega'_k := \Omega'(\beta_k), \\ &\left(\lambda_1\Phi'^{\top}_k P\Phi'_k + \lambda_2\Omega'^{\top}_k\Omega'_k + \tau_k L^{\top}L\right)z_k = -\left\{\lambda_1\Phi'^{\top}_k P\Phi_k + \lambda_2\Omega'^{\top}_k(\Omega_k - \sigma) + \tau_k L^{\top}L(\beta_k - \bar{\beta})\right\} \\ &\beta_{k+1} = \beta_k + \mu_k z_k,\end{aligned} \tag{2.10}$$

where $\{\tau_k\}$ is the regularization sequence and L is a linear operator from a Hilbert space H to a real Hilbert space H_3. The sequence $\{\mu_k\}$ stands for the step size, while $\bar{\beta}$ is a reference value for the unknown parameter, β. In practical implementation, it is assumed that the observation operators, Φ and Ω, are fitted to v and σ, some noise contaminated measurements for two data sets, $\hat{v}$ and $\hat{\sigma}$, respectively. The standard assumptions on $\{\tau_k\}$,

$$\tau_k \geq \tau_{k+1} > 0, \quad \bar{\tau} := \sup_{k=0,1,2,\ldots}\sqrt{\frac{\tau_k}{\tau_{k+1}}} < \infty, \quad \text{and} \quad \lim_{k\to\infty}\tau_k = 0 \tag{2.11}$$

guarantee that, given the right choice of initial approximations, the regularization is sufficient to ensure stability, but not excessive [20,21]. The sequence $\{\mu_k\}$ can be chosen by a backtracking line search procedure [24] with an upper bound on the number of the search steps that would enforce the lower bound on μ_k:

$$0 < \mu \leq \mu_k \leq 1. \tag{2.12}$$

Since parameter estimation problems are generally unstable and the reported data are corrupt, iteratively regularized projected Gauss–Newton algorithm (2.10) is expected to be semi-convergent, which means it has to be terminated early. To that end, we adopt the following *a posteriori* stopping rule

$$\begin{aligned}&\max\left\{\|P\Phi_{\mathcal{K}_\delta}\|^2, \|\Omega_{\mathcal{K}_\delta} - \sigma\|^2\right\} < \rho\delta \leq \max\left\{\|P\Phi_k\|^2, \|\Omega_k - \sigma\|^2\right\}, \quad 0 \leq k < \mathcal{K}_\delta, \\ &c := \max\left\{1, 2\|\Phi(\hat{\beta})\|\right\} < \sqrt{\rho},\end{aligned} \tag{2.13}$$

that is, iterations are terminated at the first index $k = \mathcal{K}_\delta$, for which $\max\left\{\|P\Phi_k\|^2, \|\Omega_k - \sigma\|^2\right\}$ is less than $\rho\delta$.

3. Convergence analysis

Of primary interest in our convergence analysis is the case where the functional in (2.5) is vanishing for exact data, $\hat{v}$ and $\hat{\sigma}$, that is, there is some element $\hat{\beta} \in H$ (maybe nonunique) such that

$$\left\{ \frac{\lambda_1}{2} \left\| \hat{P}\Phi(\hat{\beta}) \right\|^2 + \frac{\lambda_2}{2} \left\| \Omega(\hat{\beta}) - \hat{\sigma} \right\|^2 \right\} = \inf_{\beta \in H} \left\{ \frac{\lambda_1}{2} \left\| \hat{P}\Phi(\beta) \right\|^2 + \frac{\lambda_2}{2} \| \Omega(\beta) - \hat{\sigma} \|^2 \right\} = 0 \tag{3.1}$$

with $\hat{P} := E - \hat{v}(\hat{v}, \cdot)$ and $\hat{v} := \dfrac{\hat{\eta}}{\|\hat{\eta}\|}$. Suppose that nonlinear operators Φ and Ω act between real Hilbert spaces H and H_1 and H and H_2, respectively, i.e., $\Phi : H \to H_1$ and $\Omega : H \to H_2$, and that Φ and Ω are Fréchet differentiable in $\mathcal{U}_\zeta(\hat{\beta}) := \{q \in H : \|q - \hat{\beta}\| \le \zeta\}$ without such structural assumptions as monotonicity, invertibility of $\Phi'^{\top}(\cdot)\Phi'(\cdot)$ and/or $\Omega'^{\top}(\cdot)\Omega'(\cdot)$ etc. The radius of the neighborhood, ζ, is specified in the statement of Theorem 1 below. Let the following conditions hold:

$$\max \left\{ \|\Phi'(q)\|, \|\Omega'(q)\| \right\} \le M_1 \quad \text{for any} \quad q_1 \in \mathcal{U}_\zeta(\hat{\beta}), \tag{3.2}$$

$$\max \left\{ \|\Phi'(q) - \Phi'(h)\|, \|\Omega'(q) - \Omega'(h)\| \right\} \le M_2 \|q - h\| \quad \text{for any} \quad q, h \in \mathcal{U}_\zeta(\hat{\beta}). \tag{3.3}$$

Define $\mathcal{F}(M_1, M_2)$ to be the class of operators Φ and Ω satisfying (3.2) and (3.3). The crucial part of the convergence analysis of algorithm (2.10) is the following lemma.

Lemma 1. *Assume that for a linear operator L acting between real Hilbert spaces H and H_3, the operator $L^{\top}L$ is surjective and there is a constant $m > 0$ such that*

$$(L^{\top}Lh, h) \ge m\|h\|^2 \quad \textit{for any} \quad h \in H. \tag{3.4}$$

Let nonlinear operators Φ and Ω be Fréchet differentiable in $\mathcal{U}_\zeta(\hat{\beta})$ with $\zeta > 0$, and λ_1, λ_2, and τ be some positive constants. Then the inverse operator, $[\lambda_1\Phi'^{\top}(\beta)P\Phi'(\beta) + \lambda_2\Omega'^{\top}(\beta)\Omega'(\beta) + \tau L^{\top}L]^{-1}$, exists and the following inequalities hold

$$\left\| [\lambda_1\Phi'^{\top}(\beta)P\Phi'(\beta) + \lambda_2\Omega'^{\top}(\beta)\Omega'(\beta) + \tau L^{\top}L]^{-1} \right\| \le \frac{1}{\tau m}, \tag{3.5}$$

$$\left\| [\lambda_1\Phi'^{\top}(\beta)P\Phi'(\beta) + \lambda_2\Omega'^{\top}(\beta)\Omega'(\beta) + \tau L^{\top}L]^{-1}\lambda_1\Phi'^{\top}(\beta)P \right\| \le \frac{1}{2}\sqrt{\frac{\lambda_1}{\tau m}}, \tag{3.6}$$

$$\left\| [\lambda_1\Phi'^{\top}(\beta)P\Phi'(\beta) + \lambda_2\Omega'^{\top}(\beta)\Omega'(\beta) + \tau L^{\top}L]^{-1}\lambda_2\Omega'^{\top}(\beta) \right\| \le \frac{1}{2}\sqrt{\frac{\lambda_2}{\tau m}}. \tag{3.7}$$

Proof of Lemma 1. According to (2.9) and (3.4), for arbitrary $\tau > 0$ and $\beta, h \in H$, one has

$$\left([\lambda_1\Phi'^{\top}(\beta)P\Phi'(\beta) + \lambda_2\Omega'^{\top}(\beta)\Omega'(\beta) + \tau L^{\top}L]h, h \right) \ge \tau m\|h\|^2.$$

Therefore, $[\lambda_1\Phi'^{\top}(\beta)P\Phi'(\beta) + \lambda_2\Omega'^{\top}(\beta)\Omega'(\beta) + \tau L^{\top}L]^{-1}$ exists and (3.5) holds, which implies that iterations (2.10) are well-defined. To estimate the norm of

$$T_1 := [\lambda_1\Phi'^{\top}(\beta)P\Phi'(\beta) + \lambda_2\Omega'^{\top}(\beta)\Omega'(\beta) + \tau L^{\top}L]^{-1}\lambda_1\Phi'^{\top}(\beta)P, \tag{3.8}$$

we note that for any bounded linear operator in a Hilbert space a polar decomposition is satisfied. Hence

$$P\Phi'(\beta) = U|P\Phi'(\beta)|,$$

where $|P\Phi'(\beta)| := ((P\Phi'(\beta))^{\top}P\Phi'(\beta))^{1/2} = (\Phi'^{\top}(\beta)P\Phi'(\beta))^{1/2}$ and U is a partial isometry:

$$\|Uq\| = \|q\| \quad \forall q \in \mathcal{N}(U)^{\perp} \quad \text{and} \quad \mathcal{N}(U) := \{q : Uq = 0\}.$$

Denote

$$A := \Phi'^{\top}(\beta)P\Phi'(\beta), \quad B = \lambda_2\Omega'^{\top}(\beta)\Omega'(\beta) + \tau L^{\top}L, \quad \text{and} \quad C := A^{1/2}B^{-1/2},$$

Then (3.8) and condition (3.4) yield

$$\begin{aligned} T_1 = (\lambda_1 A + B)^{-1}\lambda_1 A^{1/2}U^{\top} &= [B^{1/2}(\lambda_1 B^{-1/2}AB^{-1/2} + E)B^{1/2}]^{-1}\lambda_1 A^{1/2}U^{\top} \\ &= B^{-1/2}(\lambda_1 C^{\top}C + E)^{-1}\lambda_1 C^{\top}U^{\top}. \end{aligned} \tag{3.9}$$

Writing $C = V|C| = V(C^{\top}C)^{1/2}$, where V is a partial isometry, and applying the spectral theorem to the self-adjoint operator $C^{\top}C$, one concludes

$$\begin{aligned} \|T_1\| \le \|B^{-1/2}\| \, \|(\lambda_1 C^{\top}C + E)^{-1}\lambda_1 C^{\top}\| \, \|U^{\top}\| &\le \|B^{-1/2}\| \, \|(\lambda_1 C^{\top}C + E)^{-1}\lambda_1 (C^{\top}C)^{1/2}\| \, \|V^{\top}\| \\ &\le \frac{1}{\sqrt{\tau m}} \max_{t \ge 0} \frac{\lambda_1\sqrt{t}}{\lambda_1 t + 1} = \frac{1}{2}\sqrt{\frac{\lambda_1}{\tau m}}. \end{aligned} \tag{3.10}$$

This proves (3.6). Using a similar argument with $A := \Omega'^{\top}(\beta)\Omega'(\beta)$, $B := \lambda_1\Phi'^{\top}(\beta)P\Phi'(\beta) + \tau L^{\top}L$ and $C := A^{1/2}B^{-1/2}$, one obtains (3.7).

Remark 1. A special case of IRPGN algorithm (2.10) with $L = E$, the identity operator in H, was first introduced and studied numerically in [5]. The penalty term for $L = E$ corresponds to the original Tikhonov's $\mathcal{L}_2$-regularization, $\tau_k\|\beta_k - \bar{\beta}\|^2$. However, for some diseases, the inherently differing scales of biological parameters may complicate their simultaneous recovery by a regularized optimization algorithm based on the original Tikhonov's functional. For example, in the case of avian influenza H5N1 virus, the unknown transmission rate consists of two sub-vectors, the bird-to-human transmission rate, $\beta_b(t)$, and the bird-to-bird transmission rate, $\beta_r(t)$. The bird-to-human transmission rate, $\beta_b(t)$, is of order 10^{-8} or 10^{-7}, while the bird-to-bird transmission rate, $\beta_r(t)$, is of order 10^{-3} [25–27] (data related to humans and poultry is in units 10^5 and 10^7 individuals, respectively; time is in months). With these two parameters being 5 or 4 orders of magnitude apart, the sensitivities of the cost functional with respect to each variable is also on different scales, which prevents their simultaneous recovery. This suggests that the regularization on $\beta_b(t)$ should be appropriately weighted through a more general Tikhonov's penalty term, $\|L(\beta_k - \bar{\beta})\|^2$, to ensure convergence in both variables. A much needed flexibility afforded by the penalty term $\|L(\beta_k - \bar{\beta})\|^2$ also allows to incorporate other types of problem-specific *a priori* information, which is not covered by the operators Φ, Ω, or the data, $\hat{\eta}$ and $\hat{\sigma}$. In certain cases, L maps spline expansion coefficients for the discrete analog of $\beta(t)$ to the physical space, where the unknown solution is actually defined. In other cases, L encodes statistical assumptions about the components of $\beta(t)$ based on the values of their neighbors [22].

We now formulate our basic convergence result for iteratively regularized algorithm (2.10) combined with stopping rule (2.13).

Theorem 1. *1. Let assumptions of Lemma 1 hold with nonlinear operators Φ and Ω being Fréchet differentiable in the class $\mathcal{F}(M_1, M_2)$, where $\zeta = l\sqrt{\tau_0}$ and l is given by (3.14) below.*

2. The regularization sequence $\{\tau_k\}$ and the step size sequence $\{\mu_k\}$ are chosen according to (2.11) and (2.12), respectively.

3. The modified source condition [28]

$$L^* L(\hat{\beta} - \bar{\beta}) \in \lambda_2 \Omega'^{\top}(\hat{\beta}) S, \quad S := \{v \in H_2,\ \|v\| \le \varepsilon\} \tag{3.11}$$

is satisfied.

4. Exact data sets, $\hat{v}$ and $\hat{\sigma}$, are given by their noise contaminated measurements, v and σ:

$$\max\{\|v - \hat{v}\|,\ \|\sigma - \hat{\sigma}\|\} \le \delta. \tag{3.12}$$

5. Nonlinear operators Φ and Ω and IRPGN iterations (2.10) are constrained by the following inequalities

$$\frac{\lambda_2 M_2 \varepsilon}{m} + \frac{\bar{\tau} - 1}{\bar{\tau}\mu} + \sqrt{\frac{\varepsilon}{m}\left\{\frac{(\sqrt{\lambda_1\lambda_2} + \lambda_2)M_2}{2} + \frac{M_1^2(2\|\Phi(\hat{\beta})\|\sqrt{\lambda_1\lambda_2} + \lambda_2)}{(\sqrt{\rho} - c)^2}\right\}} \le 1, \tag{3.13}$$

where $c := \max\left\{1, 2\|\Phi(\hat{\beta})\|\right\} < \sqrt{\rho}$, and the initial value of the regularization parameter, τ_0, is selected in such a way that

$$\frac{\|\beta_0 - \hat{\beta}\|}{\sqrt{\tau_0}} \le \frac{\varepsilon\sqrt{\lambda_2}}{\sqrt{m}\left\{1 - \frac{\lambda_2 M_2 \varepsilon}{m} - \frac{\bar{\tau} - 1}{\bar{\tau}\mu}\right\}} := l. \tag{3.14}$$

Then

1. For iterations (2.10), the following estimate holds

$$\frac{\|\beta_k - \hat{\beta}\|}{\sqrt{\tau_k}} \le l, \quad k = 0, 1, \dots, \mathcal{K}_\delta, \tag{3.15}$$

where $\mathcal{K}_\delta$ is calculated by a posteriori rule (2.13).

2. The sequence $\{\mathcal{K}_\delta\}$ is admissible, i.e.

$$\lim_{\delta\to 0}\|\beta_{\mathcal{K}_\delta} - \tilde{\beta}\| = 0, \quad \text{where} \quad \tilde{\beta} = \operatorname*{argmin}_{\beta\in\mathcal{U}_\zeta^\circ(\hat{\beta})}\left\{\frac{\lambda_1}{2}\left\|\hat{P}\Phi(\beta)\right\|^2 + \frac{\lambda_2}{2}\|\Omega(\beta) - \hat{\sigma}\|^2\right\}. \tag{3.16}$$

Proof of Theorem 1. Suppose for any j, $0 \le j < k < \mathcal{K}_\delta$, the induction assumption is fulfilled:

$$e_j := \frac{\|\beta_j - \hat{\beta}\|}{\sqrt{\tau_j}} \le l. \tag{3.17}$$

Since the nonlinear operators Φ and Ω are in the class $\mathcal{F}(M_1, M_2)$ and $\hat{P}\Phi(\hat{\beta}) = 0$, one has

$$P\Phi_k = (P - \hat{P})\Phi(\hat{\beta}) + P\Phi_k'(\beta_k - \hat{\beta}) + P\mathcal{B}_1(\beta_k, \hat{\beta}), \tag{3.18}$$

$$\Omega_k - \sigma = \hat{\sigma} - \sigma + \Omega_k'(\beta_k - \hat{\beta}) + \mathcal{B}_2(\beta_k, \hat{\beta}), \tag{3.19}$$

$$\max\left\{\|P\mathcal{B}_1(\beta_k, \hat{\beta})\|, \|\mathcal{B}_2(\beta_k, \hat{\beta})\|\right\} \le \frac{M_2}{2}\|\beta_k - \hat{\beta}\|^2. \tag{3.20}$$

Considering that P is an orthogonal projection and $\hat{P}\Phi(\hat{\beta}) = 0$ according to (2.10) and (3.1), one concludes $(P - \hat{P})\Phi(\hat{\beta}) = P(P - \hat{P})\Phi(\hat{\beta})$. Hence

$$\begin{aligned}\beta_{k+1} - \hat{\beta} &= (1-\mu_k)(\beta_k - \hat{\beta}) - \mu_k \left(\lambda_1 \Phi_k'^{\top} P \Phi_k' + \lambda_2 \Omega_k'^{\top} \Omega_k' + \tau_k L^{\top} L\right)^{-1} \Big\{ \lambda_1 \Phi_k'^{\top} P \big[(P - \hat{P})\Phi(\hat{\beta}) \\ &+ \mathcal{B}_1(\beta_k, \hat{\beta})\big] + \lambda_2 \Omega_k'^{\top} \left[\hat{\sigma} - \sigma + \mathcal{B}_2(\beta_k, \hat{\beta}) + \tau_k v\right] \Big\} - \lambda_2 \mu_k \tau_k \left(\lambda_1 \Phi_k'^{\top} P \Phi_k' + \lambda_2 \Omega_k'^{\top} \Omega_k' \right. \\ &+ \left. \tau_k L^{\top} L\right)^{-1} \left[\Omega'(\hat{\beta}) - \Omega_k'\right]^{\top} v. \end{aligned} \tag{3.21}$$

Identity (3.21) along with inequalities (3.5)–(3.7) yield

$$\begin{aligned}\|\beta_{k+1} - \hat{\beta}\| &= (1-\mu_k)\|\beta_k - \hat{\beta}\| + \mu_k \sqrt{\frac{\lambda_1}{\tau_k m}} \left[\|P - \hat{P}\| \, \|\Phi(\hat{\beta})\| + \|\mathcal{B}_1(\beta_k, \hat{\beta})\|\right] \\ &+ \mu_k \sqrt{\frac{\lambda_2}{\tau_k m}} \left[\|\hat{\sigma} - \sigma\| + \|\mathcal{B}_2(\beta_k, \hat{\beta})\| + \tau_k \|v\|\right] + \frac{\lambda_2 \mu_k \varepsilon}{m} \|\Omega'(\hat{\beta}) - \Omega_k'\|. \end{aligned} \tag{3.22}$$

To estimate $\|P - \hat{P}\|$, note that according to (3.12) for any $h \in H$ one has

$$\begin{aligned}\|(P - \hat{P})h\| &= \|v(v,h) - \hat{v}(\hat{v},h)\| \le \|v\| \, \|(v,h) - (\hat{v},h)\| + \|v - \hat{v}\| \, \|(\hat{v},h)\| \\ &\le (\|v\| + \|\hat{v}\|)\|v - \hat{v}\| \, \|h\| \le 2\delta \|h\|. \end{aligned} \tag{3.23}$$

By stopping rule (2.13), two cases are possible:

1. $\sqrt{\rho\delta} \le \|\Omega_k - \sigma\| \le \|\Omega_k - \Omega(\hat{\beta})\| + \|\sigma - \hat{\sigma}\| \le M_1 \|\beta_k - \hat{\beta}\| + \delta$. Without loss of generality one can assume $\delta < 1$. Therefore, $\sqrt{\rho\delta} - \sqrt{\delta} \le \sqrt{\rho\delta} - \delta \le M_1 \|\beta_k - \hat{\beta}\| + \delta$ and $\delta \le \frac{M_1^2 \|\beta_k - \hat{\beta}\|^2}{(\sqrt{\rho} - 1)^2}$.
2. $\sqrt{\rho\delta} \le \|P\Phi_k\| \le \|P\Phi_k - P\Phi(\hat{\beta})\| + \|P - \hat{P}\| \, \|\Phi(\hat{\beta})\| \le M_1 \|\beta_k - \hat{\beta}\| + 2\delta \, \|\Phi(\hat{\beta})\|$. This implies $\delta \le \frac{M_1^2 \|\beta_k - \hat{\beta}\|^2}{(\sqrt{\rho} - 2\|\Phi(\hat{\beta})\|)^2}$. In either case,

$$\delta \le \frac{M_1^2 \|\beta_k - \hat{\beta}\|}{(\sqrt{\rho} - c)^2} \quad \text{with} \quad c := \max\left\{1, 2\|\Phi(\hat{\beta})\|\right\} < \sqrt{\rho} \quad \text{as in (2.13).} \tag{3.24}$$

From (3.22)–(3.24) together with (2.11) one concludes

$$\begin{aligned}\frac{\|\beta_{k+1} - \hat{\beta}\|}{\sqrt{\tau_{k+1}}} &\le \bar{\tau} \left(1 - \mu_k \left(1 - \frac{\lambda_2 M_2 \varepsilon}{m}\right)\right) \frac{\|\beta_k - \hat{\beta}\|}{\sqrt{\tau_k}} + \frac{\mu_k \bar{\tau}}{2\sqrt{m}} \left\{ \frac{(\sqrt{\lambda_1} + \sqrt{\lambda_2}) M_2}{2} \right. \\ &+ \left. \frac{M_1^2 (2\|\Phi(\hat{\beta})\| \sqrt{\lambda_1} + \sqrt{\lambda_2})}{(\sqrt{\rho} - c)^2} \right\} \frac{\|\beta_k - \hat{\beta}\|^2}{\tau_k} + \frac{\mu_k \bar{\tau}}{2} \sqrt{\frac{\lambda_2}{m}} \varepsilon. \end{aligned} \tag{3.25}$$

By induction assumption (3.17) and inequality and (3.25), one has

$$\begin{aligned}e_{k+1} &\le \bar{\tau} \left(1 - \mu_k \left(1 - \frac{\lambda_2 M_2 \varepsilon}{m}\right)\right) l + \frac{\mu_k \bar{\tau}}{2\sqrt{m}} \left\{ \frac{(\sqrt{\lambda_1} + \sqrt{\lambda_2}) M_2}{2} + \frac{M_1^2 (2\|\Phi(\hat{\beta})\| \sqrt{\lambda_1} + \sqrt{\lambda_2})}{(\sqrt{\rho} - c)^2} \right\} l^2 \\ &+ \frac{\mu_k \bar{\tau}}{2} \sqrt{\frac{\lambda_2}{m}} \varepsilon. \end{aligned} \tag{3.26}$$

Estimate (3.26) and condition (3.13) imply (3.15). To show that the sequence $\mathcal{K} = \mathcal{K}_\delta$ is admissible we notice that, according to (2.13), $\mathcal{K}_\delta$ is nondecreasing as $\delta \to 0$. If for any $\delta \le \delta_0$, the stopping time remains constant, that is, $\mathcal{K}_\delta = \mathcal{K}_0$, then by (3.12) and (2.13), one obtains

$$\lim_{\delta \to 0} \beta_{\mathcal{K}_\delta}(v, \sigma) = \operatorname*{argmin}_{\beta \in \mathcal{U}_\zeta^*(\hat{\beta})} \left\{ \frac{\lambda_1}{2} \left\| \hat{P}\Phi(\beta) \right\|^2 + \frac{\lambda_2}{2} \|\Omega(\beta) - \hat{\sigma}\|^2 \right\}.$$

If, on the other hand, $\mathcal{K}_\delta \to \infty$ as $\delta \to 0$, then

$$\|\beta_{\mathcal{K}_\delta} - \hat{\beta}\| \le l \sqrt{\tau_{\mathcal{K}_\delta}} \to 0 \quad \text{as} \quad \delta \to 0.$$

Thus in both cases $\beta_{\mathcal{K}_\delta}$ converges in the norm of H to $\operatorname{argmin}_{\beta \in \mathcal{U}_\zeta^*(\hat{\beta})} \left\{ \frac{\lambda_1}{2} \left\| \hat{P}\Phi(\beta) \right\|^2 + \frac{\lambda_2}{2} \|\Omega(\beta) - \hat{\sigma}\|^2 \right\}$ as $\delta \to 0$. This completes the proof. □

4. Biological model and numerical simulations

In this section, we focus on numerical simulations that illustrate the efficiency of the proposed algorithm (2.10) in the reconstruction of incidence reporting rate during the Delta wave of COVID-19 pandemic in the US. To that end, we consider

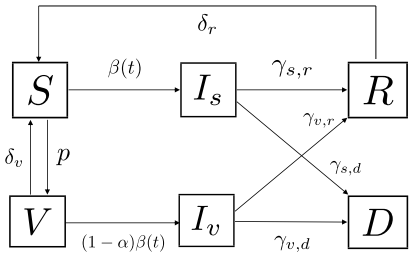

Fig. 1. Transmission diagram of the SVI_sI_vRD model (4.1)–(4.6).

nonlinear minimization problem (2.1) constrained by the SVI_sI_vRD compartmental model that was first introduced in [11] and further studied in [5] (see Fig. 1 for the transmission diagram). The model incorporates development and widespread distribution of Moderna, Pfizer-BioNTech, and Johnson & Johnson vaccines prior to the start of SARS-CoV-2 Delta variant. The SVI_sI_vRD model [11] divides susceptible and infected population into vaccinated and unvaccinated categories to account for varying virus dynamics, such as disease transmission, recovery and death rates, within these two groups [29–31]. The model has 6 compartments: susceptible unvaccinated (S), susceptible vaccinated (V), infected unvaccinated (I_s), infected vaccinated (I_v), recovered (R), and deceased (D). Given a relatively short period of study (from July 9, 2021, to November 25, 2021), we assume that population changes due to birth, immigration, death of causes rather than COVID-19, etc. are all balanced out, and that at any given time, t, the population of the region is $N - D(t)$, where N is the population at $t = 0$, that is, $N = S(0) + V(0) + I_s(0) + I_v(0) + R(0) + D(0)$.

$$\frac{\partial S}{\partial t} = -\beta(t)\frac{S(t)}{N - D(t)}(I_s(t) + I_v(t)) - pS(t) + \delta_r R(t) + \delta_v V(t) \tag{4.1}$$

$$\frac{\partial V}{\partial t} = pS(t) - (1-\alpha)\beta(t)\frac{V(t)}{N - D(t)}(I_s(t) + I_v(t)) - \delta_v V(t) \tag{4.2}$$

$$\frac{\partial I_s}{\partial t} = \beta(t)\frac{S(t)}{N - D(t)}(I_s(t) + I_v(t)) - (\gamma_{s,r} + \gamma_{s,d})I_s(t) \tag{4.3}$$

$$\frac{\partial I_v}{\partial t} = (1-\alpha)\beta(t)\frac{V(t)}{N - D(t)}(I_s(t) + I_v(t)) - (\gamma_{v,r} + \gamma_{v,d})I_v(t) \tag{4.4}$$

$$\frac{\partial R}{\partial t} = \gamma_{s,r} I_s(t) + \gamma_{v,r} I_v(t) - \delta_r R(t) \tag{4.5}$$

$$\frac{\partial D}{\partial t} = \gamma_{s,d} I_s(t) + \gamma_{v,d} I_v(t) \tag{4.6}$$

From Eqs. (4.1) and (4.2), one concludes that the daily number of newly infected people is equal to $\beta\frac{(I_s[\beta] + I_v[\beta])}{N - D[\beta]}(S[\beta] + (1-\alpha)V[\beta])$ while, according to (4.6), the daily number of individuals deceased due to COVID-19 is $\gamma_{s,d} I_s[\beta] + \gamma_{v,d} I_v[\beta]$. Therefore, the observation operators for incidence cases, $\hat{\eta}$, and daily new deaths, $\hat{\sigma}$, are defined, respectively, as

$$\Phi(\beta) := \beta\frac{(I_s[\beta] + I_v[\beta])}{N - D[\beta]}(S[\beta] + (1-\alpha)V[\beta]) \quad \text{and} \quad \Omega(\beta) := \gamma_{s,d} I_s[\beta] + \gamma_{v,d} I_v[\beta]. \tag{4.7}$$

In our numerical experiments, the goal was to apply the novel iteratively regularized preconditioned Gauss–Newton (IRPGN) algorithm (2.10) along with the stopping rule (2.13) to estimate the unknown transmission rate, $\beta(t)$, in order to compute the incidence reporting rate, $\Psi = \frac{\|\hat{\eta}\|^2}{(\hat{\eta}, \Phi(\beta))}$, and the effective reproduction number

$$\mathcal{R}_e(t) = \frac{\beta(t)}{N - D(t)}\left(\frac{S(t)}{\gamma_{s,r} + \gamma_{s,d}} + \frac{(1-\alpha)V(t)}{\gamma_{v,r} + \gamma_{v,d}}\right),$$

for model (4.1)–(4.6), which plays a crucial role in assessing the scope of the disease and the efficiency of prevention measures [11, 32–34]. When $\mathcal{R}_e(t) > 1$, each infected individual, on average, is transmitting the disease to more than one other person, i.e., the pandemic is on the rise. Conversely, when $\mathcal{R}_e(t) < 1$, the transmission is declining as each infected person is passing the disease to fewer than one other human.

For all regions considered, the vaccination rate, p, was pre-estimated based on CDC data [11,35] by dividing the change in the percentage of vaccinated people at the start and at the end of the study window by the length of the study window (140 days), see Table 3 for details. The vaccine effectiveness, α, was set at 0.8, since the age-standardized crude vaccine effectiveness (VE) for Delta variant was reported at 80% during July–November of 2021 [11,36].

Following [11], the death rate for unvaccinated individuals, $\gamma_{s,d}$, was calculated using the infectious fatality ratio $IFR = 0.5\%$ [37] and the median time from illness onset to death $\mathcal{T} = 18.5$ days [38], that is, $\gamma_{s,d} = 0.005/18.5 = 0.00027$ days^{-1}. The death rate for vaccinated individuals, $\gamma_{v,d}$, was estimated to be much smaller, $\gamma_{v,d} = \gamma_{s,d}/12.7 = 0.000021$ days^{-1}, since according to [39], unvaccinated people had 12.7 times the risks for COVID-19–associated death as compared to vaccinated ones [11]. Based on the values of $\gamma_{s,d}$ and $\gamma_{v,d}$ and using a recovery period of 10 days, the recovery rates for unvaccinated and vaccinated humans

Table 1
Comparison of reconstructed reporting rates from incidence and cumulative data for SARS CoV-2 Delta variant COVID-19 from July 9 to November 25, 2021 - IRPGN algorithm.

States	Reconstructed reporting rate from incidence data	Reconstructed reporting rate from cumulative data
Colorado	0.242(95%CI:[0.232,0.252])	0.249(95%CI:[0.247,0.25])
Idaho	0.166(95%CI:[0.157,0.176])	0.150(95%CI:[0.149,0.151])
Indiana	0.212(95%CI:[0.203,0.221])	0.203(95%CI:[0.202,0.204])
Massachusetts	0.279(95%CI:[0.266,0.294])	0.270(95%CI:[0.268,0.273])
Michigan	0.392(95%CI:[0.377,0.41])	0.374(95%CI:[0.371,0.377])
Minnesota	0.331(95%CI:[0.314,0.35])	0.322(95%CI:[0.318,0.325])
Nevada	0.141(95%CI:[0.136,0.146])	0.121(95%CI:[0.12,0.122])
New York	0.330(95%CI:[0.317,0.343])	0.306(95%CI:[0.304,0.308])
South Carolina	0.181(95%CI:[0.176,0.187])	0.185(95%CI:[0.184,0.185])
Tennessee	0.279(95%CI:[0.272,0.287])	0.263(95%CI:[0.262,0.264])
Washington	0.208(95%CI:[0.202,0.215])	0.210(95%CI:[0.209,0.211])
Wyoming	0.199(95%CI:[0.185,0.214])	0.192(95%CI:[0.189,0.195])
USA Total	0.237(95%CI:[0.236,0.238])	0.207(95%CI:[0.205,0.208])

Table 2
Comparison of reconstructed reporting rates using LSQCURVFIT and IRPGN algorithms with incidence and cumulative data - SARS - CoV-2 Delta variant, July 9 - November 25, 2021.

States	Reconstructed reporting rate from incidence data (IRPGN)	Reconstructed reporting rate from incidence data (LSQCURVFIT)	Reconstructed reporting rate from cumulative data (IRPGN)	Reconstructed reporting rate from cumulative data (LSQCURVFIT)
Colorado	0.24225	0.25335	0.24855	0.25191
Idaho	0.16584	0.17054	0.14985	0.15191
Indiana	0.21236	0.20107	0.20281	0.21135
Massachusetts	0.27943	0.28459	0.27046	0.26989
Michigan	0.39232	0.38067	0.37366	0.37696
Minnesota	0.33070	0.33310	0.32210	0.32303
Nevada	0.14053	0.13345	0.12094	0.11997
New York	0.33017	0.3235	0.30079	0.30213
South Carolina	0.18132	0.16743	0.18451	0.18025
Tennessee	0.27947	0.28406	0.26292	0.25911
Washington	0.20808	0.20562	0.21037	0.21170
Wyoming	0.19948	0.19857	0.19187	0.19333
USA Total	0.23678	0.23306	0.20654	0.20635

Table 3
Population data as of July 1, 2021 [40], and proportion of vaccinated individuals for different states of the US [41].

States	Population-Estimation 2021 as of July 1	Vaccination percentage as of 7/9/21	Vaccination percentage as of 11/25/21	Vaccination rate, p, between 7/9/21-11/25/21
Colorado	5,784,865	52.6	62.9	0.000735714
Idaho	1,849,202	36.5	45.1	0.000614286
Indiana	6,788,799	42.9	50.5	0.000542857
Massachusetts	6,995,729	62.4	70.8	0.0006
Michigan	10,069,577	47.7	54.4	0.000478571
Minnesota	5,709,852	52.5	62.2	0.000692857
Nevada	3,115,648	42.7	54.2	0.000821429
New York	20,108,296	55.1	68.2	0.000935714
South Carolina	5,131,848	39.3	51.2	0.00085
Tennessee	6,925,619	37.8	49.4	0.000828571
Washington	7,724,031	55.7	64.8	0.00065
Wyoming	577,605	35.6	45.3	0.000692857
USA Total	331,893,745	47.7	60.6	0.000921429

were pre-estimated as $\gamma_{s,r} = (1-0.005)/10 = 0.0995$ days^{-1} and $\gamma_{v,r} = (1-0.005/12.7)/10 = 0.09996$ days^{-1}, respectively [11]. Finally, the loss of immunity rate for recovered individuals, δ_r, was set at $\delta_r = 1/90 = 0.011$ days^{-1}, and the loss of immunity rate for vaccinated individuals, δ_v, was set at 0 considering that in the early 2021, Moderna and Pfizer-BioNTech vaccines offered immunity against SARS-CoV-2 Delta variant for at least 6 month and most people in the US got vaccinated shortly before the beginning of the study period (or later) [11].

To discretize the unknown transmission rate, $\beta(t)$ was projected onto a finite-dimensional subspace spanned by shifted Legendre polynomials, $P_1(t)$, $P_2(t)$, …, $P_m(t)$. This gives rise to a finite-dimensional approximation, $\tilde{\beta}[\theta]$, in the form $\tilde{\beta}[\theta](t) = \sum_{j=1}^{m} \theta_j P_j(t)$. At every step of the iterative process (2.10), the nonlinear ODE system (4.1)–(4.6) was solved numerically using Matlab R2023a built-in function ode23s with $\beta = \tilde{\beta}[\theta]$. In that manner, state variables, $\tilde{S}[\theta]$, $\tilde{V}[\theta]$, $\tilde{I}_s[\theta]$, $\tilde{I}_v[\theta]$, $\tilde{R}[\theta]$, and $\tilde{D}[\theta]$, have been obtained

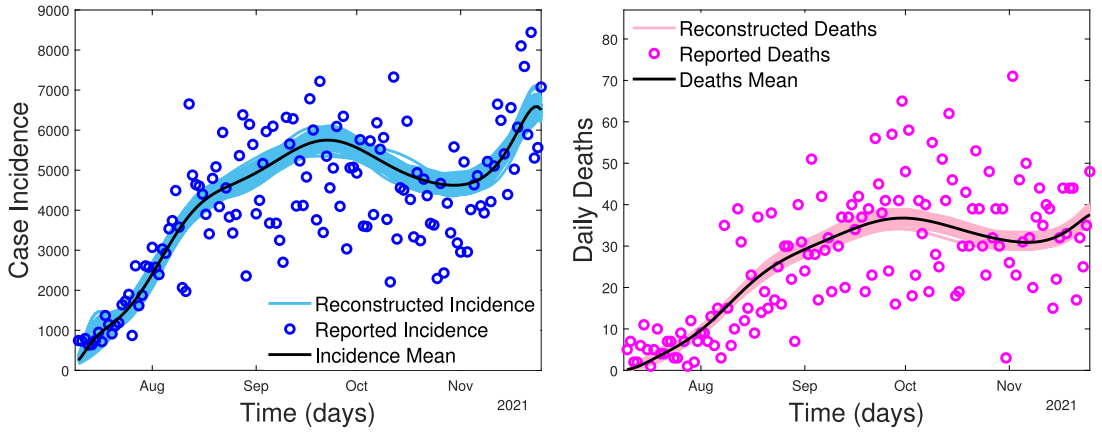

Fig. 2. Data fit to incidence cases (left) and daily new deaths (right) for the state of New York - SARS - CoV-2 Delta variant, July 9 - November 25, 2021 - IRPGN algorithm.

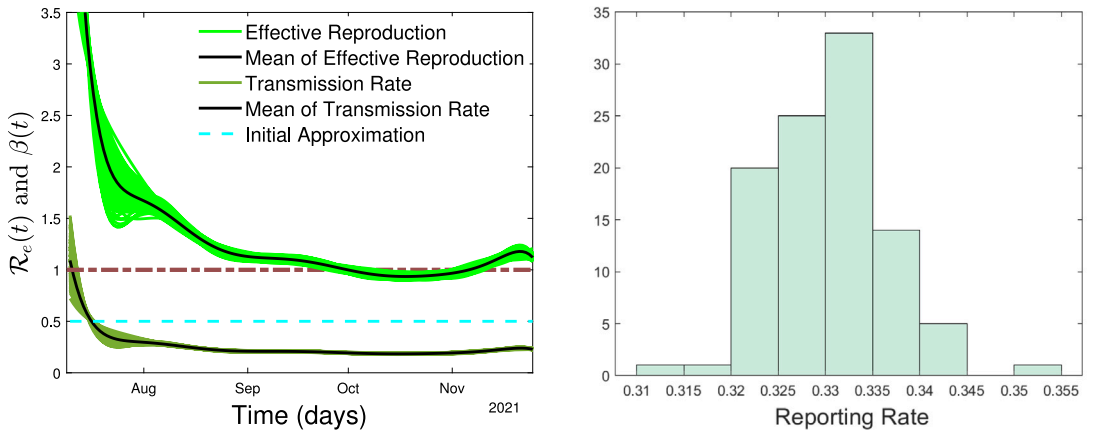

Fig. 3. Reconstructed effective reproduction number, $\mathcal{R}_e(t)$, and disease transmission rate, $\beta(t)$, (left) along with the reconstructed reporting rate, $\Psi = 1/\psi$, (right) for the state of New York - SARS - CoV-2 Delta variant, July 9 - November 25, 2021 - IRPGN algorithm.

as functions of the expansion coefficients, θ, which led to discrete analogs of the observation operators, Φ and Ω in (4.7). In order to quantify uncertainty in the extracted $\vec{\beta}$, $\vec{\mathcal{R}}_e$, and Ψ, the model was refitted (using parallel programming *parfor* option in Matlab R2023a) to $M = 100$ additional data sets for incidence cases and daily deaths assuming Poisson error structure. The resulting M best-fit parameter sets were used to plot the histograms for the reconstructed reporting rates, Ψ, as illustrated in Figs. 3 and 5, along with the 95% confidence intervals, shown in Table 1.

All experiments have been conducted based on data for daily new infections and deaths between July 9, 2021, and November 25, 2021, from the Centers for Disease Control and Prevention [9] and from Johns Hopkins University (JHU) [10]. Whenever raw data appeared to be corrupt due to inconsistent reporting (no reporting or under-reporting over the weekends and holidays, for example), a 7-day moving average has been employed by averaging data from three days before and after a specific day. A detailed information on the source of each data set for all 50 states in the US is presented in Table 6.

For comparison, numerical simulations were also carried out with cumulative data of reported cases and deaths. The reporting rates, Ψ, calculated from both daily and cumulative data sets for all 50 states deviated by no more than 3%. A lineup of reconstruction results for 12 different states with a broad range of population sizes [40] and vaccination percentages [41] is illustrated in Table 3. Overall, our experiments show that between July 9, 2021, and November 25, 2021, most states in the US had incidence reporting rate between 15% and 25%.

To double-check the values of Ψ approximated by IRPGN method (2.10), Matlab R2023a built-in least square curve fitting (LSQCURVFIT) procedure has also been employed, and simulations have been carried out using both incidence and cumulative data sets. The estimates of Ψ, obtained by IRPGN and LSQCURVFIT for the same 12 states as in Table 1, are summarized in Table 2. Our analysis indicates that the reporting rates derived from incidence and cumulative data sets are very similar for both the IRPGN and LSQCURVFIT algorithms. For most states, the rates, Ψ, based on incidence data are slightly higher, but the difference is within 3%.

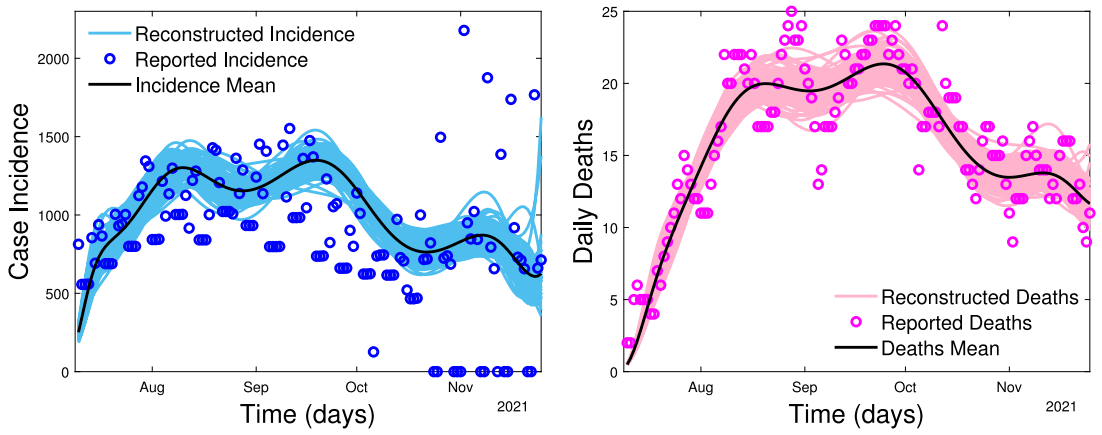

Fig. 4. Data fit to incidence cases (left) and 7-day moving average for daily new deaths (right) for the state of Nevada - SARS - CoV-2 Delta variant, July 9 - November 25, 2021 - IRPGN algorithm.

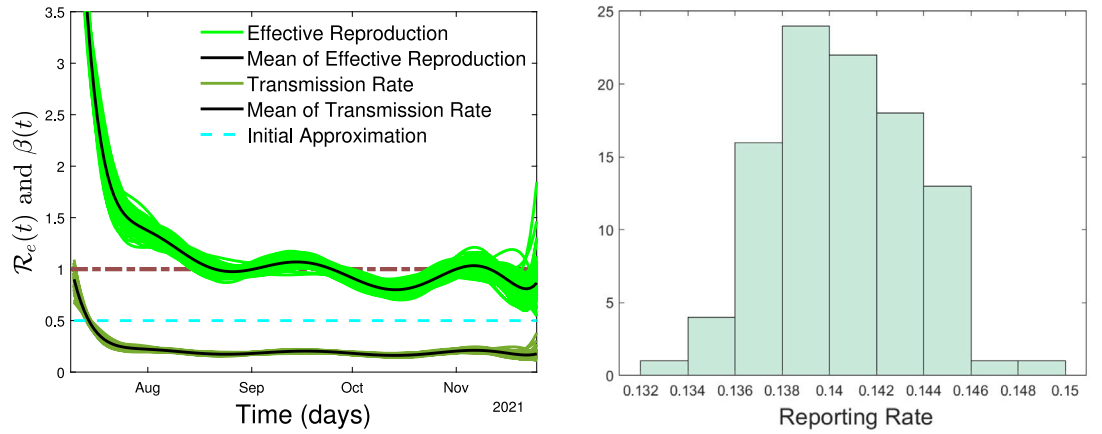

Fig. 5. Reconstructed effective reproduction number, $\mathcal{R}_e(t)$, and disease transmission rate, $\beta(t)$, (left) along with the reconstructed reporting rate, $\Psi = 1/\psi$, (right) for the state of Nevada - SARS - CoV-2 Delta variant, July 9 - November 25, 2021 - IRPGN algorithm.

An obvious argument in favor of incidence data is independence and identical distribution (i.i.d.) of errors. On the flip side, incidence data may be a rather chaotic aggregation of multiple epidemic sub-waves, which is hard to fit. Cumulative data, on the other hand, is smooth and easy to fit, but they suffer from the dominance of earlier cases and growing noise propagation. Taking into account all pros and cons of both types of data sets, we believe that reconfirming estimation results with incidence and cumulative data is the best strategy.

Reconstructions with IRPGN algorithm using data on incidence cases and daily new deaths from JHU [10] between July 9 and November 25, 2021, for the state of New York are illustrated in Figs. 2 and 3. Simulation results for the state of Nevada with IRPGN algorithm have been obtained with incidence data for daily new infections and 7-day moving average for daily new deaths from CDC [9], see Figs. 4 and 5. The uphill trend in the incidence data for the state of New York towards the end of the study period is reflected in the estimated effective reproduction number, $\mathcal{R}_e(t)$.

In the state of Nevada, on the other hand, the outbreak remains contained up until the end of the study period, which is consistent with the reconstructed $\mathcal{R}_e(t)$. A sharp increase in the number of daily new cases in the state of New York towards the end of November, 2021, is probably due to the emergence of SARS-CoV-2 Omicron variant even though officially Omicron cases have not been reported in the US until December, 2021. In terms of the estimated reporting rates, Ψ, the two states are on the different sides of the spectrum, with New York reporting rate being one of the highest among all 50 states and Nevada reporting rate being one of the lowest.

As evident from Table 2, the estimates of the reporting rate, Ψ, obtained with algorithms IRPGN and LSQCURVFIT are very consistent, which makes it hard to designate the winner. The IRPGN procedure is superior when it comes to the radius of convergence. Since a disease transmission rate, by definition, takes values from 0 to 1, a reasonable unbiased choice of $\beta_0(t)$ was $\beta_0(t) = 0.5$, that is, $\theta = [0.5, 0, 0, \dots, 0]^\top$. With IRPGN method, this initial approximation worked for all 50 states in the US. When $\beta_0(t) = 0.5$ was not close to the unknown minimizer, one had to select a larger value of τ_0. However, since $\tau_k \to 0$ as $k \to \infty$, this

Table 4
Regularization sequences, $\{\tau_k\}$, and stopping times, $\mathcal{K}_\delta$, for different states in the US - IRPGN algorithm.

States	Regularization sequence $\{\tau_k\}$ for incidence data	Stopping time $\mathcal{K}_\delta$ for incidence data	Regularization sequence $\{\tau_k\}$ for cumulative data	Stopping time $\mathcal{K}_\delta$ for cumulative data
Colorado	$\tau_k = 5\times 10^{-2}/(k+1)^6$	$\mathcal{K}_\delta = 15$	$\tau_k = 3/(k+1)^{3.5}$	$\mathcal{K}_\delta = 15$
Idaho	$\tau_k = 10^{-5}/(k+1)^{0.7}$	$\mathcal{K}_\delta = 10$	$\tau_k = 10^{-1}/(k+1)^{0.1}$	$\mathcal{K}_\delta = 15$
Indiana	$\tau_k = 3\times 10^{-8}/(k+1)^{0.7}$	$\mathcal{K}_\delta = 15$	$\tau_k = 3\times 10^{-4}/(k+1)^{0.1}$	$\mathcal{K}_\delta = 15$
Massachusetts	$\tau_k = 9\times 10^{-8}/(k+1)^{1.09}$	$\mathcal{K}_\delta = 15$	$\tau_k = 4\times 10^{-4}/(k+1)^{1.4}$	$\mathcal{K}_\delta = 15$
Michigan	$\tau_k = 10^3/(k+1)^7$	$\mathcal{K}_\delta = 15$	$\tau_k = 10/(k+1)^3$	$\mathcal{K}_\delta = 15$
Minnesota	$\tau_k = 8\times 10^{-8}/(k+1)^{0.9}$	$\mathcal{K}_\delta = 18$	$\tau_k = 4\times 10^{-4}/(k+1)^{1.2}$	$\mathcal{K}_\delta = 15$
Nevada	$\tau_k = 10^{-5}/(k+1)^{1.2}$	$\mathcal{K}_\delta = 10$	$\tau_k = 1/(k+1)^{1.9}$	$\mathcal{K}_\delta = 10$
New York	$\tau_k = 10^3/(k+1)^4$	$\mathcal{K}_\delta = 10$	$\tau_k = 3\times 10^3/(k+1)^6$	$\mathcal{K}_\delta = 10$
South Carolina	$\tau_k = 20^{-4}/(k+1)^{1.5}$	$\mathcal{K}_\delta = 20$	$\tau_k = 2/(k+1)^{0.4}$	$\mathcal{K}_\delta = 15$
Tennessee	$\tau_k = 10^{-5}/(k+1)^{3.9}$	$\mathcal{K}_\delta = 20$	$\tau_k = 1/(k+1)^5$	$\mathcal{K}_\delta = 15$
Washington	$\tau_k = 10^{-8}/(k+1)^{1.5}$	$\mathcal{K}_\delta = 10$	$\tau_k = 5/(k+1)^6$	$\mathcal{K}_\delta = 15$
Wyoming	$\tau_k = 10^{-5}/(k+1)^{0.3}$	$\mathcal{K}_\delta = 15$	$\tau_k = 1/(k+1)^{0.6}$	$\mathcal{K}_\delta = 15$
USA Total	$\tau_k = 9/(k+1)^{2.7}$	$\mathcal{K}_\delta = 15$	$\tau_k = 50/(k+1)^{1.3}$	$\mathcal{K}_\delta = 35$

Table 5
Weighting coefficients, λ_1 and λ_2, for LSQCURVFIT and IRPGN algorithms using incidence and cumulative data.

States	Weighting coefficient of incidence data IRPGN	Weighting coefficient of incidence data LSQCURVFIT	Weighting coefficient of cumulative data IRPGN	Weighting coefficient of cumulative data LSQCURVFIT
Colorado	$\lambda_1 = 10^{-8},\ \lambda_2 = 5\times 10^{-6}$	$\lambda_1 = 3,\ \lambda_2 = 4000$	$\lambda_1 = 10^{-7},\ \lambda_2 = 2.5\times 10^{-5}$	$\lambda_1 = 0.34,\ \lambda_2 = 100$
Idaho	$\lambda_1 = .33\times 10^{-7},\ \lambda_2 = .33\times 10^{-4}$	$\lambda_1 = 0.22,\ \lambda_2 = 170$	$\lambda_1 = 5\times 10^{-7},\ \lambda_2 = 10^{-5}$	$\lambda_1 = 0.18,\ \lambda_2 = 30$
Indiana	$\lambda_1 = 10^{-9},\ \lambda_2 = 2\times 10^{-7}$	$\lambda_1 = 0.25,\ \lambda_2 = 50$	$\lambda_1 = 2.5\times 10^{-9},\ \lambda_2 = 2.5\times 10^{-7}$	$\lambda_1 = 0.27,\ \lambda_2 = 100$
Massachusetts	$\lambda_1 = 10^{-8},\ \lambda_2 = 2.5\times 10^{-6}$	$\lambda_1 = 0.4,\ \lambda_2 = 80$	$\lambda_1 = 1.67\times 10^{-9},\ \lambda_2 = 1.25\times 10^{-6}$	$\lambda_1 = 0.37,\ \lambda_2 = 230$
Michigan	$\lambda_1 = 3.33\times 10^{-8},\ \lambda_2 = 2\times 10^{-5}$	$\lambda_1 = 0.6,\ \lambda_2 = 150$	$\lambda_1 = 10^{-7},\ \lambda_2 = 3.33\times 10^{-5}$	$\lambda_1 = 0.61,\ \lambda_2 = 200$
Minnesota	$\lambda_1 = 3.33\times 10^{-10},\ \lambda_2 = 3.33\times 10^{-7}$	$\lambda_1 = 0.5,\ \lambda_2 = 350$	$\lambda_1 = 1.67\times 10^{-9},\ \lambda_2 = 3.33\times 10^{-6}$	$\lambda_1 = 0.48,\ \lambda_2 = 300$
Nevada	$\lambda_1 = 2\times 10^{-8},\ \lambda_2 = .25\times 10^{-4}$	$\lambda_1 = 0.13,\ \lambda_2 = 30$	$\lambda_1 = 1.67\times 10^{-7},\ \lambda_2 = 1.67\times 10^{-4}$	$\lambda_1 = 0.14,\ \lambda_2 = 130$
New York	$\lambda_1 = 3.33\times 10^{-8},\ \lambda_2 = 2\times 10^{-5}$	$\lambda_1 = 0.45,\ \lambda_2 = 120$	$\lambda_1 = 5\times 10^{-8},\ \lambda_2 = 1.43\times 10^{-5}$	$\lambda_1 = 0.44,\ \lambda_2 = 260$
South Carolina	$\lambda_1 = 1.43\times 10^{-7},\ \lambda_2 = 2\times 10^{-5}$	$\lambda_1 = 0.2,\ \lambda_2 = 30$	$\lambda_1 = 10^{-6},\ \lambda_2 = 10^{-5}$	$\lambda_1 = 0.22,\ \lambda_2 = 40$
Tennessee	$\lambda_1 = 2\times 10^{-9},\ \lambda_2 = 3.33\times 10^{-7}$	$\lambda_1 = 0.4,\ \lambda_2 = 70$	$\lambda_1 = 3.33\times 10^{-9},\ \lambda_2 = 3.33\times 10^{-7}$	$\lambda_1 = 0.35,\ \lambda_2 = 60$
Washington	$\lambda_1 = 1.25\times 10^{-11},\ \lambda_2 = 3.03\times 10^{-8}$	$\lambda_1 = 0.2,\ \lambda_2 = 300$	$\lambda_1 = 5\times 10^{-9},\ \lambda_2 = 1.11\times 10^{-6}$	$\lambda_1 = 0.27,\ \lambda_2 = 60$
Wyoming	$\lambda_1 = 5\times 10^{-7},\ \lambda_2 = 5\times 10^{-5}$	$\lambda_1 = 0.25,\ \lambda_2 = 30$	$\lambda_1 = 3.33\times 10^{-6},\ \lambda_2 = 5\times 10^{-5}$	$\lambda_1 = 0.24,\ \lambda_2 = 40$
USA Total	$\lambda_1 = 33\times 10^{-9},\ \lambda_2 = 17\times 10^{-6}$	$\lambda_1 = 0.27,\ \lambda_2 = 90$	$\lambda_1 = 33\times 10^{-9},\ \lambda_2 = 33\times 10^{-8}$	$\lambda_1 = 0.26,\ \lambda_2 = .5$

did not have any negative impact on the accuracy of the reconstruction. In the case of LSQCURVFIT, the value 0.5 did not work for all states (even with large initial damping) and a broad range of values from $[0.1, 0.5]$ had to be adopted.

Overall, the ability to choose the regularization sequence, $\{\tau_k\}$, makes the IRPGN algorithm user-friendly and rather easy to implement, even for heavily noise contaminated data. The regularization sequences presented in Table 4 are near optimal. However a wide range of parameters can be utilized to ensure convergence. For example, the regularization sequence for COVID-19 daily incidence cases and deaths in Massachusetts is $\tau_k = 9\times 10^{-8}/(k+1)^{1.09}$, but the power of denominator can be replaced by any value in $[0.1, 3]$. For all 50 states in the US, in the case of IRPGN scheme, numerical experiments were carried out with $L = E$, the identity operator in the Hilbert space H. This choice of L produced the most stable results. At the same time, mapping θ to the corresponding function, $\tilde{\beta}[\theta](t) = \sum_{j=1}^{m} \theta_j P_j(t)$, that is, $L : \theta \to \tilde{\beta}[\theta]$, also worked.

Furthermore, the problem-specific nature of IRPGN method made it easier to adjust the weights assigned to incidence cases, λ_1, and daily new deaths, λ_2; see Table 5. In general, states with similar populations had very similar values of λ_1 and λ_2. On the other hand, finding the best weights, λ_1 and λ_2, when using LSQCURVFIT was a more tricky and time-consuming endeavor and made the algorithm harder to implement as compared to IRPGN (see Table 5).

5. Conclusions and discussion

To be strategic and efficient in our responses to future epidemic outbreaks, it is important to develop biological models and numerical algorithms for stable estimation of crucial disease parameters such as transmission and reporting rates. These parameters are influenced by multiple genetic, environmental, and social factors, which makes it impossible to assess their values through any direct computation. Thus a carefully regularized optimization procedure needs to be used to estimate transmission and reporting rates from noise-contaminated data. In this paper, we present a robust iteratively regularized computational algorithm applicable to a broad class of nonlinear minimization problems constrained by various disease-specific (networked) compartmental models. A rigorous theoretical analysis of the proposed numerical scheme coupled with an *a posteriori* stopping rule has been conducted.

Table 6
Sources of SARS-CoV-2 Delta variant COVID-19 data on daily new cases and deaths by state.

State	Incidence data source	Death data source
Alabama	Daily incidence [9]	Daily death [9]
Alaska	7-day average [9]	7-day average [9]
Arizona	Daily incidence [9]	Daily death [9]
Arkansas	Daily incidence [9]	Daily death [9]
California	7-day average [11]	7-day average [11]
Colorado	Daily incidence [9]	Daily death [9]
Connecticut	7-day average [9]	7-day average [9]
Delaware	Daily incidence [9]	Daily death [9]
Florida	Daily incidence [9]	Daily death [9]
Georgia	Daily incidence [9]	Daily death [9]
Hawaii	7-day average [9]	7-day average [9]
Idaho	Daily incidence [9]	7-day average [9]
Illinois	7-day average [9]	7-day average [9]
Indiana	7-day average [9]	7-day average [9]
Iowa	7-day average [9]	7-day average [9]
Kansas	7-day average [9]	7-day average [9]
Kentucky	Daily incidence [9]	Daily death [9]
Louisiana	7-day average [9]	7-day average [9]
Maine	7-day average [9]	7-day average [9]
Maryland	Daily incidence [9]	Daily death [9]
Massachusetts	7-day average [9]	7-day average [9]
Michigan	7-day average [9]	7-day average [9]
Minnesota	7-day average [9]	7-day average [9]
Mississippi	7-day average [9]	7-day average [9]
Missouri	7-day average [9]	7-day average [9]
Montana	7-day average [9]	7-day average [9]
Nebraska	7-day average [9]	7-day average [9]
Nevada	Daily incidence [9]	7-day average [9]
New Hampshire	7-day average [9]	7-day average [9]
New Jersey	Daily incidence [9]	Daily death [9]
New Mexico	7-day average [9]	7-day average [9]
New York	Daily incidence [10]	Daily death [10]
North Carolina	Daily incidence [9]	Daily death [9]
North Dakota	7-day average [9]	7-day average [9]
Ohio	Daily incidence [9]	7-day average [10]
Oklahoma	7-day average [9]	7-day average [9]
Oregon	7-day average [9]	7-day average [9]
Pennsylvania	Daily incidence [9]	Daily death [9]
Rhode Island	7-day average [9]	7-day average [9]
South Carolina	7-day average [9]	7-day average [9]
South Dakota	7-day average [9]	7-day average [10]
Tennessee	7-day average [9]	7-day average [9]
Texas	Daily incidence [9]	Daily death [9]
Utah	7-day average [9]	7-day average [9]
USA	Daily incidence [10]	Daily death [10]
Vermont	7-day average [9]	7-day average [9]
Virginia	7-day average [9]	7-day average [10]
Washington	Daily incidence [9]	Daily death [9]
West Virginia	7-day average [9]	7-day average [9]
Wisconsin	7-day average [9]	7-day average [9]
Wyoming	7-day average [9]	7-day average [9]

Numerical simulations carried out with a SVI_sI_vRD biological model [11] and real data for Delta variant of COVID-19 pandemic in different states of the US [9,10] confirm our theoretical findings and illustrate practical advantages of the proposed algorithm.

The immediate goal for our future research is to introduce optimal forecasting and control strategies that would capitalize on parameter estimation results afforded by algorithm (2.10), (2.13). The datasets generated during and/or analyzed during the current study are available from the corresponding author on reasonable request.

Data availability

Data will be made available on request.

References

[1] Martí Català, David Pino, Miquel Marchena, Pablo Palacios, Tomás Urdiales, Pere-Joan Cardona, Sergio Alonso, David López-Codina, Clara Prats, Enrique Alvarez-Lacalle, Robust estimation of diagnostic rate and real incidence of COVID-19 for European policymakers, PLoS One 16 (1) (2021) e0243701.

[2] Chao Wu, Cong Xu, Feng Mao, Xiaolin Xu, Chan Zhang, The impact of invisible-spreaders on COVID-19 transmission and work resumption, PLoS ONE 17 (1) (2022) e0252994.

[3] Hazhir Rahmandad, Tse Yang Lim, John Sterman, Behavioral dynamics of COVID-19: estimating underreporting, multiple waves, and adherence fatigue across 92 nations, Syst. Dyn. Rev. 37 (1) (2021) 5–31.

[4] Ruiyun Li, Sen Pei, Bin Chen, Yimeng Song, Tao Zhang, Wan Yang, Jeffrey Shaman, Substantial undocumented infection facilitates the rapid dissemination of novel coronavirus (SARS-CoV-2), Science 368 (6490) (2020) 489–493.

[5] A. Smirnova, M. Baroonian, Reconstruction of incidence reporting rate for SARS-CoV-2 delta variant of COVID-19 pandemic in the US, Infect. Dis. Model. 9 (1) (2023) 70–83.

[6] G. Chowell, H. Nishiura, Transmission dynamics and control of ebola virus disease (EVD): a review, BMC Med. 196 (2014) https://doi.org/10.1186/s12916-014-0196-0.

[7] Marisa C. Eisenberg, Suzanne L. Robertson, Joseph H. Tien, Identifiability and estimation of multiple transmission pathways in cholera and waterborne disease, J. Theoret. Biol. 324 (2013) 84–102.

[8] A. Smirnova, N. Sterrett, O.J. Mujica, C. Munayco, L. Suarez, C. Viboud, G. Chowell Spatial Dynamics, And the basic reproduction number of the great cholera epidemic in Peru, 1991–1997, PLOS Negl. Trop. Dis. 14 (2020) 7.

[9] Centers for Disease Control and Prevention, United States COVID-19 cases and deaths by state over time (ARCHIVED), 2023, https://data.cdc.gov/Case-Surveillance/Weekly-United-States-COVID-19-Cases-and-Deaths-by-/pwn4-m3yp. (Accessed 06 June 2023).

[10] Johns Hopkins University, COVID-19 deaths dataset for the United States, 2023, https://github.com/CSSEGISandData/COVID-19/blob/master/csse_covid_19_data/csse_covid_19_time_series/time_series_covid19_deaths_US.csv. (Accessed 20 June 2023).

[11] R. Luo, A.D. Herrera-Reyes, Y. Kim, S. Rogowski, D. White, A. Smirnova, Estimation of time-dependent transmission rate for COVID-19 SVIRD model using predictor-corrector algorithm, in: Mathematical Modeling for Women's Health - Collaborative Workshop for Women in Mathematical Biology, 2024, in press.

[12] R.M. Anderson, R.M. May, Infectious Diseases of Humans, Oxford University Press, 1991.

[13] J.O. Lloyd-Smith, S.J. Schreiber, P.E. Kopp, W.M. Getz, Superspreading and the effect of individual variation on disease emergence, Nature 438 (2005) 355–359.

[14] Eunha Shim, Amna Tariq, Gerardo Chowell, Spatial variability in reproduction number and doubling time across two waves of the COVID-19 pandemic in South Korea, february to july, 2020, Int. J. Infect. Dis. 102 (2021) 1–9.

[15] Giulia Giordano, Franco Blanchini, Raffaele Bruno, Patrizio Colaneri, Alessandro Di Filippo, Angela Di Matteo, Marta Colaneri, Modelling the COVID-19 epidemic and implementation of population-wide interventions in Italy, Nat. Med. 26 (6) (2020) 855–860.

[16] Kimberlyn Roosa, Yiseul Lee, Ruiyan Luo, Alexander Kirpich, Richard Rothenberg, James M Hyman, Ping Yan, Gerardo Chowell, Short-term forecasts of the COVID-19 epidemic in Guangdong and Zhejiang, China: February 13–23, 2020, J. Clin. Med. 9 (2) (2020) 596.

[17] R.N. Thompson, Epidemiological models are important tools for guiding COVID-19 interventions, BMC Med. 18 (2020) 152, https://doi.org/10.1186/s12916-020-01628-4.

[18] Qiuyue Ma, Jue Liu, Qiao Liu, Liangyu Kang, Runqing Liu, Wenzhan Jing, Yu Wu, Min Liu, Global percentage of asymptomatic SARS-CoV-2 infections among the tested population and individuals with confirmed COVID-19 diagnosis: a systematic review and meta-analysis, JAMA Netw. Open 4 (12) (2021) e2137257.

[19] Weijing Shang, Liangyu Kang, Guiying Cao, Yaping Wang, Peng Gao, Jue Liu, Min Liu, Percentage of asymptomatic infections among SARS-CoV-2 omicron variant-positive individuals: a systematic review and meta-analysis, Vaccines 10 (7) (2022) 1049.

[20] A.B. Bakushinsky, M.Yu. Kokurin, Iterative Methods for Ill-Posed Operator Equations with Smooth Operators, Springer Dordrecht, Great Britain, 2004.

[21] B. Kaltenbacher, A. Neubauer, O. Scherzer, Iterative Regularization Methods for Nonlinear Ill-Posed Problems, in: Radon Series on Computational and Applied Mathematics, Walter de Gruyter, Berlin, 2008.

[22] A. Smirnova, R.A. Renaut, T. Khan, Convergence and application of a modified iteratively regularized Gauss-Newton algorithm, Inverse Problems 23 (4) (2007) 1547–1563.

[23] A.B. Smirnova, On convergence rates for iteratively regularized procedures with a linear penalty term, Inverse Problems 28 (2012) 8.

[24] J. Nocedal, S.J. Wright, Numerical Optimization, Springer-Verlag, New York, 1999.

[25] S. Iwami, Y. Takeuchi, X. Liu, Avian-human influenza epidemic model, Math. Biosci. 207 (1) (2007) 1–25.

[26] S. Iwami, Y. Takeuchi, X. Liu, Avian flu pandemic: Can we prevent it? J. Theoret. Biol. 257 (2009) 1181–1190.

[27] N. Tuncer, M. Martcheva, Modeling seasonality in avian influenza H5N1, J. Biol. Systems 21 (4) (2013) 1340004.

[28] K. Kunisch, N. Ring, Regularization of nonlinear ill-posed problems with closed operators, Numer. Funct. Anal. Optim. 14 (1998) 389–404.

[29] Onésime Agossou, Mintodê Nicodème Atchadé, Aliou Moussa Djibril, Modeling the effects of preventive measures and vaccination on the COVID-19 spread in Benin Republic with optimal control, Results Phys. 31 (2021) 104969.

[30] M. Angeli, G. Neofotistos, M. Mattheakis, E. Kaxiras, Modeling the effect of the vaccination campaign on the COVID-19 pandemic, Chaos Solitons Fractals 154 (11162) (2022) 1.

[31] Gustavo Barbosa Libotte, Fran Sérgio Lobato, Gustavo Mendes Platt, Antônio J Silva Neto, Determination of an optimal control strategy for vaccine administration in COVID-19 pandemic treatment, Comput. Methods Programs Biomed. 196 (2020) 105664.

[32] O. Diekmann, J.A.P. Heesterbeek, J.A.J. Metz, On the definition and the computation of the basic reproduction ratio R_0 in models for infectious diseases in heterogeneous populations, J. Math. Biol. 28 (4) (1990) 365–382.

[33] P. van den Driessche, J. Watmough, Reproduction numbers and sub-threshold endemic equilibria for compartmental models of disease transmission, Math. Biosci. 180 (1–2) (2002) 29–48.

[34] Biao Tang, Xia Wang, Qian Li, Nicola Luigi Bragazzi, Sanyi Tang, Yanni Xiao, Jianhong Wu, Estimation of the transmission risk of the 2019-nCoV and its implication for public health interventions, J. Clin. Med. 9 (2) (2020) https://www.mdpi.com/2077-0383/9/2/462.

[35] CDC, Trends in number of COVID-19 vaccinations in the US, 2022, https://covid.cdc.gov/covid-data-tracker/#vaccination-trends. (Accessed 30 September 2021).

[36] CDC, Morbidity and mortality weekly report, 2022, https://www.cdc.gov/mmwr/volumes/71/wr/mm7104e2.htm.

[37] M. O'Driscoll, G. Ribeiro dos Santos, L. Wang, D.A.T. Cummings, A.S. Azman, J. Paireau, A. Fontanet, S. Cauchemez, H. Salje, Age-specific mortality and immunity patterns of SARS-CoV-2, Nature 590 (2021) 140–145.

[38] Drugs.com, How do COVID-19 symptoms progress and what causes death? 2022, https://www.drugs.com/medical-answers/covid-19-symptoms-progress-death-3536264/.

[39] A.G. Johnson, COVID-19 incidence and death rates among unvaccinated and fully vaccinated adults with and without booster doses during periods of delta and omicron variant emergence—25 US jurisdictions, april 4–december 25, 2021, MMWR. Morb. Mortal. Wkly. Rep. 71 (2022).

[40] United States Census Bureau, State population totals and components of change: 2020–2022, 2023, https://www.census.gov/data/tables/time-series/demo/popest/2020s-state-total.html. (Accessed 06 June 2023).

[41] Centers for Disease Control and Prevention, Trends in number of COVID-19 vaccinations in the US, 2022.